Lithium-rich layered titanium sulfides: Cobalt- and Nickel-free high capacity cathode materials for lithium-ion batteries

Florian Flamary-Mespoulie, Adrien Boulineau, Hervé Martinez, Matthew R. Suchomel, Claude Delmas, Brigitte Pecquenard, Frédéric Le Cras

Lithium-rich layered titanium sulfides: Cobalt- and Nickel-free high capacity cathode materials for lithium-ion batteries

Florian Flamary-Mespoulie [a,b,c], Adrien Boulineau [c,d], Hervé Martinez [e], Matthew R. Suchomel [b],
Claude Delmas [b,**], Brigitte Pecquenard [b,***], Frédéric Le Cras [a,b,c,*,1]

[a] CEA, LETI, Minatec Campus, 17 Rue des Martyrs, F-38054, Grenoble, France
[b] CNRS, Université de Bordeaux, ICMCB and Bordeaux INP, F-33608, Pessac, France
[c] Université Grenoble Alpes, F-38000, Grenoble, France
[d] CEA, LITEN, 17 Rue des Martyrs, F-38054, Grenoble, France
[e] IPREM-ECP CNRS UMR 5254, Université de Pau et des Pays de L'Adour, Hélioparc Pau Pyrénées, 2 Avenue Pierre Angot, F-64053, Pau, France

ARTICLE INFO

ABSTRACT

In the context of efforts to develop at the same time high energy density cathode materials for lithium-ion batteries with low content of critical elements such as cobalt and new cell chemistries for all-solid-state batteries, a novel family of lithium-rich layered sulfides ($Li[Li_tTi_{1-t}]S_2$, $0 < t \leq 0.33$) belonging to the $LiTiS_2 – Li_2TiS_3$ system was investigated as intercalation materials. These sulfides, in which both cations and anions are involved in the redox process, display common features with isotype Li-rich layered oxides ($Li[Li_xM_{1-x}]O_2$, M = Mn, Ni, Co, …). In a particular composition range, they exhibit high electrochemical performance with a reversible capacity and an energy density exceeding respectively 265 mAh·g^{-1} and 600 Wh·kg^{-1}, a very low irreversible capacity in the first cycle, fast activation and a limited voltage decay. Their operation potential within the electrochemical stability window of sulfide-based fast ionic conductors makes them promising cathode materials for all-solid-state lithium and Li-ion batteries.

1. Introduction

While the size and quantity of lithium-ion batteries continue to expand to meet the demand of a rapidly growing electrified vehicle market, it is more necessary than ever to design new generation of lithium batteries that do not contain critical raw materials and that are intrinsically safe. An illustration of the first issue is the continuous effort made to reduce the cobalt content of the layered cathode materials, due to the high cost and the uncertain availability of the latter [1]. It is a reason why, together with a means to reach higher specific energies, NCA ($LiNi_{0.8}Co_{0.15}Al_{0.05}O_2$) and NMC-111 ($LiNi_{1/3}Mn_{1/3}Co_{1/3}O_2$) materials have been primarily used in place of $LiCoO_2$ in cells for automotive applications, and NMC-622 and possibly NMC-811 will probably replace them in turn [2]. As for batteries with intrinsic safety, all-solid-state electrochemical cells, in which the classical liquid electrolyte is substituted by a non-flammable and physically stable solid Li^+ ionic conductor, are now considered as the Holy Grail. In this context, sulfide-based inorganic ionic conductors appear as a key component of future all-solid-state batteries owing to their particularly high ionic conductivity at room temperature (up to 25.10^{-3} S cm^{-1} for $Li_{9.54}Si_{1.74}P_{1.44}S_{11.7}Cl_{0.3}$) [3,4], their low density (~2 g cm^{-3}), their ductility [5] and finally the possible absence of critical elements. The thermodynamic anodic stability limit of these electrolytes has been estimated by *ab initio* calculations not to exceed 2.5 V/Li^+/Li [6], but the practical one is found experimentally to reach up to 2.8–3.0 V/Li^+/Li [7]. The limited stability remains an issue that can be possibly circumvented either by the interposition of a thin layer of a stable Li^+ conducting and electronically insulating oxide such as $LiNbO_3$ when using conventional '4 V' layered oxide cathodes [8], or by introducing alternative cathode materials operating in the stability window and capable of delivering a very high specific capacity to compensate for the impact of a lower operating voltage on the energy density of the cell.

---

* Corresponding author. CEA, LETI, Minatec Campus, 17 rue des Martyrs, F-38054, Grenoble, France.
** Corresponding author.
*** Corresponding author.
E-mail addresses: claude-henri.Delmas@icmcb.cnrs.fr (C. Delmas), brigitte.pecquenard@icmcb.cnrs.fr (B. Pecquenard), frederic.lecras@cea.fr (F. Le Cras).
[1] Present address: CEA, LITEN, 17 rue des Martyrs, F-38054, Grenoble, France.

In this context, we report on a new family of lithium-rich layered sulfide ($Li[Li_tTi_{1-t}]S_2$, $0 < t \leq 0.33$) positive electrode materials that forms a solid solution over a large compositional range in the $LiTiS_2$–Li_2TiS_3 system, and that exhibits electrochemical behavior comparable to the one observed for layered Li-rich oxides, i.e. the presence of an initial 'high voltage' plateau and a large reversible capacity upon cycling [9]. The theoretical capacity of these Co- and Ni-free materials which are found to operate at ~2.5 V vs Li^+/Li, is up to 339 mAh.g^{-1} (Li_2TiS_3). Their theoretical specific energy is therefore of about 810 Wh.kg^{-1}, that is higher than the specific energy targeted for NMC-811 materials (750 Wh.kg^{-1}) [2]. They contain exclusively titanium as transition metal, which is abundant and which price is intermediate between the one of manganese and nickel. Besides, in so far as these compounds containing a single transition metal can be considered as a simplified system, a likely mechanism for lithium intercalation/deintercalation involving cation- and anion-based electrochemical processes can be proposed.

LiTiS$_2$ and the new crystalline Li_2TiS_3 are thus the end-members of this series of materials. $LiTiS_2$ was intensively studied in the late 1970's and early 1980's during the early chapters of Li batteries' history. It is the final product of the intercalation of lithium in TiS_2 [10–12]. $LiTiS_2$ has a 1T type structure (in the reference system used at that time [13]), equivalent to the O1 structure in the general structural designation now used for oxides [14]. It can be synthesized either by lithium intercalation in TiS_2 (electrochemical or chemical) at room temperature or by solid state reaction at high temperature. Note that a high temperature form, having the same 3R (O3) structure than $LiMO_2$ layered oxides, is metastable below 500 °C [15,16]. Regarding Li_2TiS_3, only a limited number of A_2MS_3 layered compounds are been reported in the literature, and within these known examples, only a few exhibit AM_2 honeycomb type ordering in the $[AM_2]S_2$ slabs: Li_2SnS_3 [17], Na_2ZrS_3 [18], Li_2US_3 and Na_2US_3 [19]. Besides, reversible electrochemical delithiation/lithiation was recently highlighted both in rock-salt type cubic (Fm-$3m$) Li_2TiS_3 prepared by mechanochemical synthesis [20] and in amorphous lithium titanium oxysulfides obtained by sputtering of a Li–Ti–S target [21,22]. In both cases, it was possible to electrochemically extract nearly all the lithium contained in the material during the first charge at around 2.6 V vs Li^+/Li.

2. Methods

2.1. Material syntheses

End-members of the material series were prepared at first from TiS_2 (Aldrich, 99.9%). $LiTiS_2$ was synthesized by chemical lithiation of TiS_2 at room temperature [12]. The latter was carried out in an anhydrous hexane medium using n-butyllithium (Sigma Aldrich, 1.6 M in hexane) added dropwise and TiS_2 (Sigma-Aldrich, 99.9%) in a 1.5:1 M ratio. After 5 days of reaction at 50 °C under stirring, the resulting Li_xTiS_2 powder was filtered, rinsed with fresh dry hexane in an argon filled glovebox and then dried at 120 °C under vacuum for 24 h. Li_2TiS_3 was synthesized by solid state reaction of stoichiometric amounts of TiS_2 and Li_2S. Precursors were ground and pelletized under argon. TiS_2/Li_2S pellets were placed in a glassy carbon crucible, introduced in an argon-evacuated silica ampoule, then annealed at 800 °C during 48 h and finally cooled to room temperature at -2 °C·min^{-1}. Finally, $Li[Li_tTi_{1-t}]S_2$ samples with intermediate compositions ($t = 0.04, 0.08, 0.17, 0.20, 0.25, 0.29$) were prepared in a similar way by solid state reaction of stoichiometric amounts of $LiTiS_2$ and Li_2TiS_3 precursors: $yLiTiS_2.(1-y)Li_2TiS_3$, $y=(1-3t)/(1-t)$.

2.2. Structural characterizations

High-resolution synchrotron powder diffraction (HR-SPD) measurements were performed at room temperature in a transmission capillary mode using an incident beam energy of 30 keV ($\lambda \approx 0.41$ Å) over the range 0.5–50° in 2θ, at beamline 11-BM of the Advanced Photon Source

(APS).

Analysis of the HR-SPD by the Rietveld method was performed using the TOPAS software package. The background was fit by a Chebyshev polynomial function. Peak profiles were fitted by the Fundamental Parameter (FP) approach using an instrument resolution function established from a standard LaB_6 reference sample. Peak broadening from the sample was described by combined double-Voigt Lorentzian term for crystallite size and Gaussian term for strain effects. In the standard Rietveld analysis, lattice parameters, non-special atom positions, and isotropic atom site displacement values were refined. The impact of stacking slab defects in the Li_2TiS_3 structural model was also analyzed by the TOPAS software package (version 6).

Laboratory XRD measurements were realized with a PANalytical X'Pert 3 diffractometer using Cu Kα wavelength equipped with a capillary spinner and operating at 40 mA/45 kV. The powder samples were sieved (40 μm) and sealed under argon in 0.3 mm diameter glass capillaries. XRD data analysis for structural characterizations was realized using the FullProf program [23].

HR-STEM images were recorded using a FEI Titan Ultimate microscope equipped with a monochromator and double spherical aberration
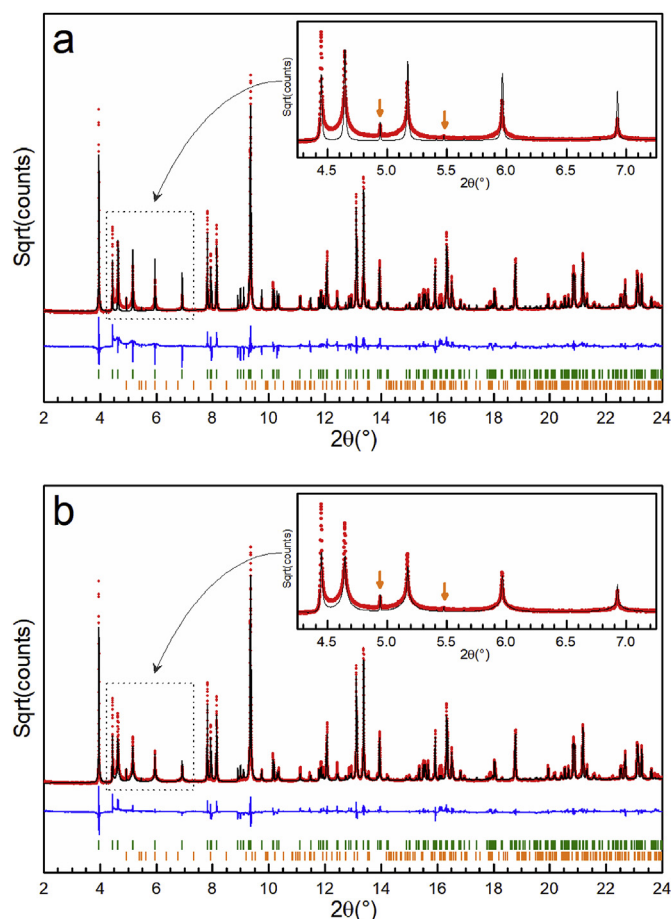
Fig. 1. Rietveld refinement fit profiles of high-resolution synchrotron powder diffraction data ($\lambda \approx 0.41$ Å) for Li_2TiS_3. a, Traditional Rietveld fit using a standard $C2/m$ model ($R_{wp} \sim 29\%$). b, Refined Li_2TiS_3 structural model incorporating stacking defects showing improved agreement with the measured data ($R_{wp} \sim 24\%$). The square root y-axis scale highlights weak intensity peaks. The improved fit of the stacking defect model is more apparent in the zoomed 2θ region for each fit (plot insets). Plots show measured data (red points), calculated profile (black line), difference curve (blue line) and hkl phase tick marks for Li_2TiS_3 (green ticks) and a minor (<2 wt%) impurity phase of Li_2TiO_3 (orange ticks, and orange arrows in plot insets). (For interpretation of the references to color in this figure legend, the reader is referred to the Web version of this article.)

correctors (Cs) for both the probe-forming and the image-forming lenses. The microscope was operating at an accelerating voltage of 200 kV using a 20 mrad convergence semi-angle. STEM images were collected using a high-angle annular dark field (HAADF) detector in Z contrast conditions.

XPS measurements were carried out by a Thermo Scientific K-Alpha X-ray photoelectron spectrometer, using a focused monochromatized Al Kα radiation (hν = 1486.6 eV). The XPS spectrometer was directly connected to a glove box under argon atmosphere in order to avoid moisture/air exposure of the samples. For the Ag 3d5/2 line, the full width at half-maximum (FWHM) was 0.50 eV under the recording conditions. The X-ray spot size was 400 μm. Peaks were recorded with constant pass energy of 20 eV. The pressure in the analysis chamber was less than 2·10^{-8} Pa. Short acquisition time spectra were recorded at the beginning and at the end of each experiment to check that the samples did not suffer from degradation during the measurements. Peak assignments were made with respect to reference compounds analyzed in the same conditions. The binding energy scale was calibrated from the hydrocarbon contamination using the C 1s peak at 285.0 eV. Core peaks were analyzed using a nonlinear Shirley-type background. The peak positions and areas were optimized by a weighted least-squares fitting method using 70% Gaussian and 30% Lorentzian line shapes. Quantification was performed on the basis of Scofield's relative sensitivity factors. For each sample, several XPS analyses were performed at different positions to make the results statistically reliable.

2.3. Electrochemical measurements

Electrode discs (14 mm diameter, loading 10 mg cm^{-2}) containing Li[Li$_t$Ti$_{1-t}$]S$_2$ 80 %wt, carbon black 7.5 %wt, graphite (KS6, Timcal) 7.5 % wt and PTFE binder 5 %wt were prepared in a glove box under argon (H$_2$O, O$_2$ < 1 ppm) using a solvent-free process. Button cells were assembled using a lithium foil (Chemetall, battery grade) as the negative electrode, a polypropylene non-woven (Viledon, Freudenberg), a microporous polypropylene membrane (Celgard 3200) as separators and the Li[Li$_t$Ti$_{1-t}$]S$_2$ based positive electrode. The electrolyte used was composed of 1 M LiTFSI dissolved in a solution of TEGDME and dioxolane in a 1:1 ratio. As a consequence of its limited anodic stability, the

maximum voltage applied to the positive electrode was limited to 3 V *vs* Li$^+$/Li. Galvanostatic measurements were performed at 25 °C using a VMP3 galvanostat-potentiostat (Bio-Logic Science Instruments) at a fixed current rate corresponding to a C/50 rate.

3. Results and discussion

### 3.1. Synthesis and structural characterization

Analysis of synchrotron powder X-ray diffraction (SP-XRD) data of the Li$_2$S:TiS$_2$ sample annealed at 800 °C, shown in Fig. 1a, reveals that a highly ordered Li$_2$TiS$_3$ phase has been obtained for the first time. Li$_2$TiS$_3$ exhibits an O3 type layered structure made of [Li$_{1/3}$Ti$_{2/3}$]S$_2$ slabs containing edge-sharing MS$_6$ octahedra (M = Ti, Li) and interslab octahedral sites exclusively occupied by Li$^+$ ions. Similarly to Li$_2$MnO$_3$, well-defined superstructure diffraction peaks are observed and originate from Li/Ti honeycomb-like ordering in the [Li$_{1/3}$Ti$_{2/3}$]S$_2$ slabs and an extensively ordered stacking sequence between successive [Li$_{1/3}$Ti$_{2/3}$]S$_2$ slabs. Therefore, the full Li$_2$TiS$_3$ SP-XRD pattern is indexed in the monoclinic system (*C2/m* space group) with the following cell parameters a = 6.1588(1) Å, b = 10.6721(2) Å, c = 6.3254(1) Å and β = 109.087(2)° (density 3.48 g cm^{-3}). Rietveld refinement of the SP-XRD pattern (Table S1), assuming the ideal packing, leads to a calculated profile of the superstructure lines that is actually slightly different from the experimental one, suggesting the presence of residual stacking defects in the slab packing. Introduction of slab glidings in the model indeed leads to a considerable improvement of the experimental fit as shown in Fig. 1b.

The lithiated phase obtained by chemical insertion of lithium in TiS$_2$ with *n*-butyllithium displays a XRD pattern consistent with a pure O1 type Li$_x$TiS$_2$ material. The values of its hexagonal cell parameters, a = 3.457 Å, c = 6.188 Å, finally confirm that a stoichiometry very close to the target LiTiS$_2$ was achieved [11,12].

Using these end-members materials, solid-state reactions between LiTiS$_2$ and Li$_2$TiS$_3$ were then carried out to successfully obtain a series of pure Li-rich layered materials over the whole compositional range Li[Li$_t$Ti$_{1-t}$]S$_2$ (0 ≤ t ≤ 0.33). The XRD patterns of the materials are compared in Fig. 2a. For small t values (t ~ 0.04), two layered phases
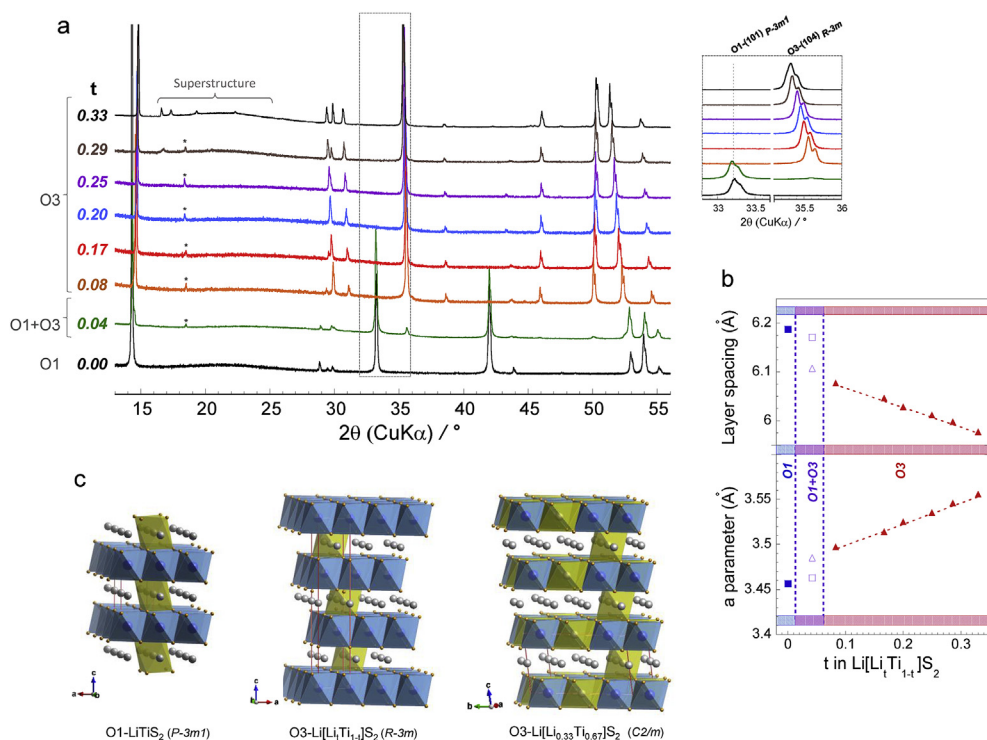
Fig. 2. Structural features of the Li[Li$_{1+t}$Ti$_{1-t}$]S$_2$ series. (a) XRD patterns (λ_{Cu}) of the Li[Li$_{1+t}$Ti$_{1-t}$]S$_2$ materials (0 ≤ t ≤ 0.33), with a zoom (inset) on O1-(101) and O3-(104) peaks (2θ range [32.7–36°]). * stands for oxide impurities Li$_4$Ti$_5$O$_{12}$ and Li$_2$TiO$_3$. (b) Lattice parameters for the series of materials. (c) Structures and unit cells of O1–LiTiS$_2$ (*P-3m1* space group), O3–Li[Li$_{1+t}$Ti$_{1-t}$]S$_2$ (*R-3m* space group) and fully-ordered O3–Li$_2$TiS$_3$ (*C2/m* space group). The unit cells are indicated with red lines. TiS$_6$ octahedra and LiS$_6$ octahedra are respectively represented in blue and yellow. (For interpretation of the references to color in this figure legend, the reader is referred to the Web version of this article.)
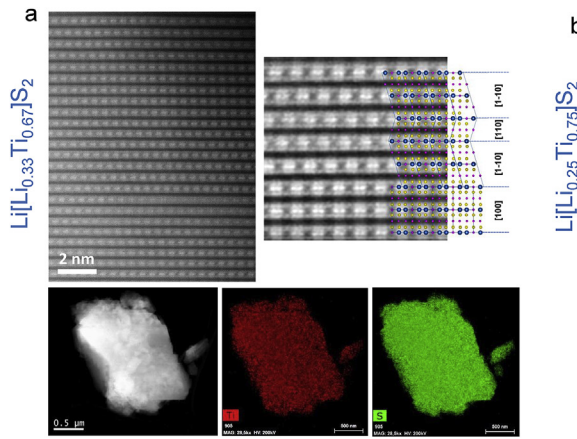
Fig. 3. Cation ordering in $Li[Li_{1+t}Ti_{1-t}]S_2$. (a) HAADF-HRSTEM image of $Li[Li_{0.33}Ti_{0.67}]S_2$ (Li_2TiS_3). Ti atoms, which can be observed as white doublets, reveal a clear Li/Ti ordering in a ratio 1:2 (Li is not visible due to its low atomic number). Stacking faults (right) revealing that the crystal is built of disoriented variants oriented along the [110] [1–8,10,11], [100] directions. EDX mapping analysis of the particle. (b) HAADF-HRSTEM image of $Li[Li_{0.25}Ti_{0.75}]S_2$ with zooms (right) on two different regions of the crystal revealing various degree of cation ordering.

with O1 and O3 structures coexist, while single-phase materials with the O3 structure form at higher t values. Superstructure peaks vanish rapidly when t deviates from the ideal maximum value of 1/3. For example, only the most intense of these peaks is still visible in conventional XRD patterns for the composition $t = 0.29$ (Fig. S1a). For lower values of t (0.25, 0.20 and 0.17), the contribution of the latter appears within the corresponding SP-XRD patterns (Fig. S1b) in the form of a broad background bump at approximately the same d-spacing, thus reflecting a persistent tendency to ordering within the $[Li_tTi_{1-t}]S_2$ slabs. Concurrently, the tendency for ordering along the c_{hex} axis is considerably reduced by intraslab disorder, which reduces the energetic favorability of ordered slab stacking.

All intermediate phases $Li[Li_tTi_{1-t}]S_2$ (~$0.08 < t < 0.33$) were indexed with a hexagonal cell (R-$3m$ space group). The cell parameter evolution follows Vegard's law (Fig. 2b), revealing a solid solution behavior. The corresponding structures of these materials are shown in Fig. 2c. In the O1 type structure ($LiTiS_2$), LiS_6 octahedra share faces with TiS_6 octahedra of the TiS_2 slabs. Indeed, the strong covalence of the Ti–S bonds, which decreases the charge borne by the titanium ions, minimizes the electrostatic repulsion with the Li^+ ions and allows octahedra face sharing. Conversely, partial substitution of titanium by lithium in $LiTiS_2$, leads to the formation of Ti^{4+} ions for charge compensation ($Li[Li^+_tTi^{4+}_{2t}Ti^{3+}_{1-3t}]S_2$). Their presence in the slab tends to destabilize the face-sharing. This leads to the formation of O3 type sulfur packing containing only edge-sharing octahedra. The existence of these two different sulfur packing arrangements explains why a two-phase region is observed for a very small excess of lithium. The increase of the a_{hex} cell parameter with t (Fig. 2b), is a consequence of the larger size of Li^+ compared to Ti^{4+} and Ti^{3+}. The interslab distance, related to the c_{hex} cell parameter, displays an abrupt change at the O1–O3 transition resulting from the disappearance of octahedra face-sharing. Subsequently, for larger t values, the c_{hex} parameter displays a progressive decrease. The cause for this trend is not clear but is probably related with the composite character of the $Li[Li_tTi_{1-t}]S_2$ materials with intermediate compositions, that are found to be an assembly of $LiTiS_2$-like and Li_2TiS_3-like nanodomains. As a consequence of this composite assembly, the value measured for the c parameter appears as a weighted average of the two contributions, and decreases linearly with t.

HAADF-STEM experiments were performed on two compositions, Li_2TiS_3 (i.e. $Li[Li_{0.33}Ti_{0.67}]S_2$) and $Li[Li_{0.25}Ti_{0.75}]S_2$, to investigate the effect of the Li:Ti ratio on the atomic arrangement (Fig. 3). High resolution HAADF images recorded for the Li_2TiS_3 end-member reveal that lithium and titanium are fully ordered within the $[Li_{1/3}Ti_{2/3}]S_2$ slabs of the typical honeycomb lattice usually observed for Li-rich layered oxides, as demonstrated by the presence of two bright dots separated by a black space which corresponds to a (Ti–Ti–Li) sequence (Fig. 3a). Honeycomb-type ordering in the $[Li_tTi_{1-t}]S_2$ slabs of Li_2TiS_3 is indeed a consequence of both the ideal 1/3 ratio for Li^+/Ti^{4+} ions and the difference in their

ionic radii (Li^+ (0.74 Å), Ti^{4+} (0.60 Å)). At the same time, as always encountered within these materials and well described for Li_2MnO_3 [24], perfect long range ordering along the c axis is not observed. Stacking faults are observed which result in variants separated by twinning planes that are rotated by $2\pi/3$ around the c_{hex} axis of the rhombohedral R-$3m$ cell. This observation is consistent with the analysis of the SP-XRD pattern (Fig. 1). Note that these structural defects do not affect the sulfur packing, which remains ABCABC, but only concern the relative positions of the successive ordered $[LiTi_2]$ layers. These planar defects are responsible for the broadening of the superstructure diffraction lines in
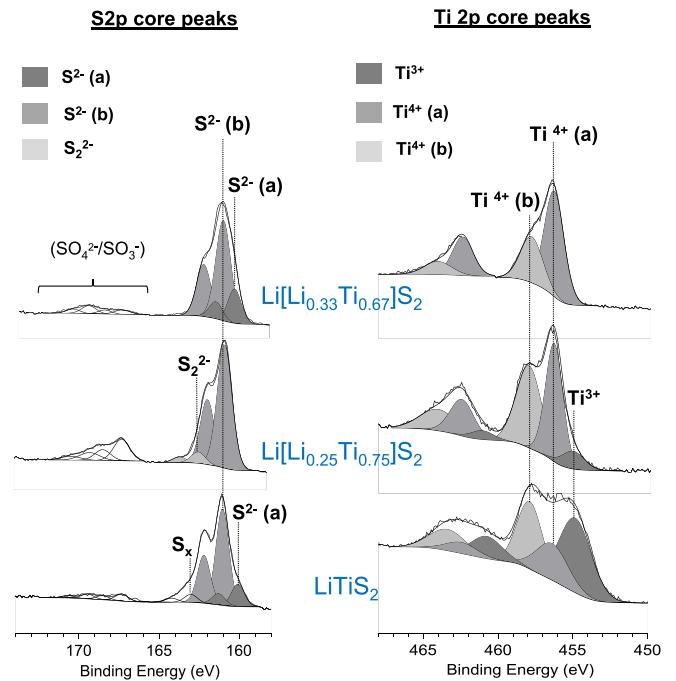

Fig. 4. XPS Ti2p and S2p spectra of pristine $LiTiS_2$, $Li[Li_{0.25}Ti_{0.75}]S_2$ and $Li[Li_{0.33}Ti_{0.67}]S_2$ materials. The S2p core peak displays one main doublet (S^{2-}(b)) at 161.0–162.2 eV assigned to S^{2-} ions as in TiS_2 or TiS_3 reference compounds. We also observe another doublet (S^{2-}(a)) at lower binding energies, which also corresponds to S^{2-} ions but with a more negative character (as in Li_2S). We also note the appearance in small proportion of polysulfides chains (S_x), sulfites and sulfates, certainly due to the presence of oxygen traces at the top surface layer of the material. The Ti2p core peak can be fitted with two or three doublets depending on the material: a doublet attributed to Ti^{3+} ions (454.8–460.8 eV), a doublet (Ti^{4+}(b)) assigned to Ti^{4+} in a sulfur environment as in TiS_2 or TiS_3 and an additional doublet (Ti^{4+}(a)) at intermediate binding energies assigned to Ti^{4+} in a mixed oxygen-sulfur environment.
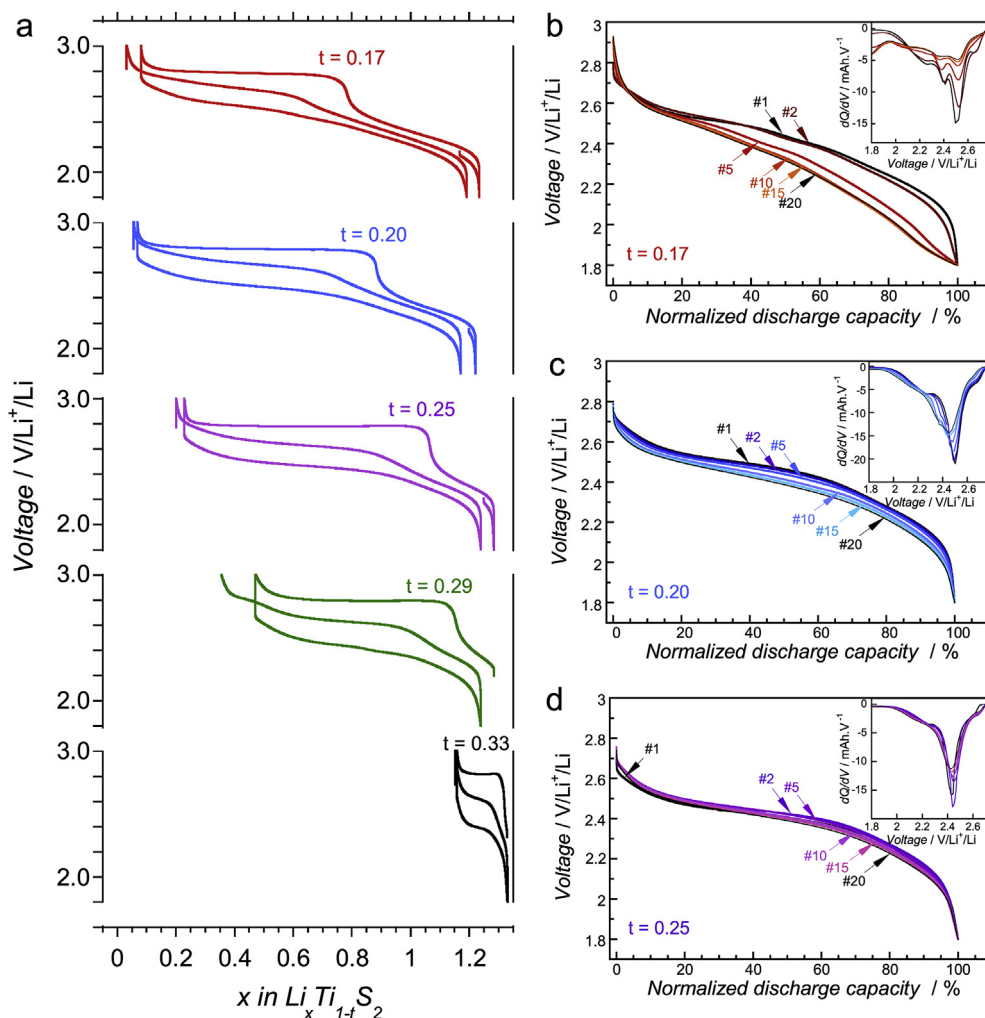
Fig. 5. Electrochemical behavior of Li[Li$_{1+t}$Ti$_{1-t}$]S$_2$. (a) Voltage profiles for the Li[Li$_{1+t}$Ti$_{1-t}$]S$_2$ series in lithium metal cells. Discharge curves and corresponding ∂(capacity)/∂V curves (insets) for cycles 1 to 20 for Li$_{1.17}$Ti$_{0.83}$S$_2$ (b), Li$_{1.20}$Ti$_{0.80}$S$_2$ (c), and Li$_{1.25}$Ti$_{0.75}$S$_2$ (d).

the powder SP-XRD pattern. For compositions in the solid solution with t < 0.33, some smaller titanium ions are necessarily located in the Li site of the ideal honeycomb lattice and therefore should prevent ideal ordering. HAADF-STEM analysis of the intermediate Li[Li$_{0.25}$Ti$_{0.75}$]S$_2$ phase reveals the layered structure of this material and its inhomogeneous character (Fig. 3b). Indeed, while local cation ordering in the [Li$_t$Ti$_{1-t}$]S$_2$ slabs (*i.e.* Li$_2$TiS$_3$-like nano-domains) is visible in some areas of the crystal, it is absent in some other areas. This short coherence length in the partially ordered slabs observed in the Li[Li$_{0.25}$Ti$_{0.75}$]S$_2$ material is thus likely responsible for the absence of $C2/m$ superstructure X-ray diffraction peaks.

XPS analyses of the pristine Li[Li$_t$Ti$_{1-t}$]S$_2$ materials (Fig. 4 and Table S2) confirm that: (i) mainly divalent S^{2-} ions are present, (ii) Ti^{3+} species appear for values of t less than 0.33 and (iii) the fraction of Ti^{3+} grows as t decreases in agreement to the general formula Li[Li^+_tTi$^{4+}_{2t}$ Ti$^{3+}_{1-3t}$]S$_2$. The presence of Ti^{4+} in the XPS spectrum of LiTiS$_2$ highlights the strong affinity of titanium for oxygen, combined with an extreme surface analysis for which oxygen traces could not be avoided (even if strict experimental atmosphere conditions are used) leading to difficulties to observe reduced states of titanium ions [25]. This behavior is frequently observed with reduced materials, as for example NaVO$_2$, in which V^{3+} has a strong tendency to oxidize, and leads to the spontaneous
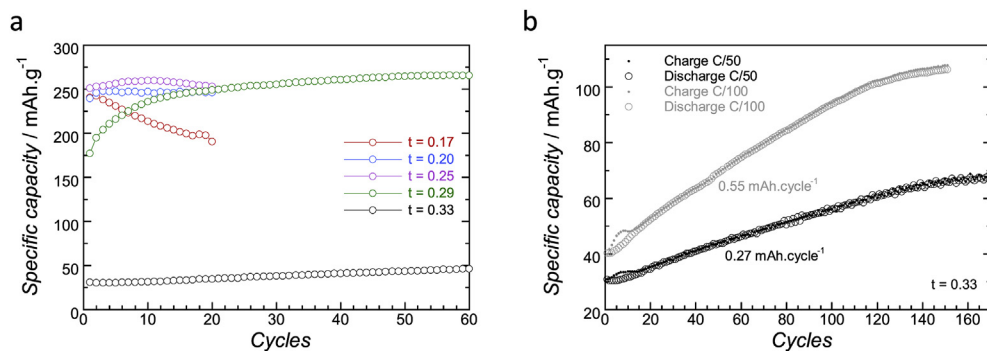
Fig. 6. (a) Evolution of the specific capacity of Li[Li$_{1+t}$Ti$_{1-t}$]S$_2$ materials (C/50 rate, [1.8–3.0]V vs Li$^+$/Li, 25 °C). (b) Evolution of the specific capacity of Li$_2$TiS$_3$ during prolonged cycling at C/50 and C/100. As shown in Fig. S3, the linear increase observed for Li$_2$TiS$_3$ is consistent with the incremental activation of a thin layer (typically few nm thick) of the material at each cycle, while the change in the slope probably results from the activation of a sample having a bi-modal particle size distribution.

formation of a $Na_{1-x}VO_2$ phase [26,27].

3.2. Electrochemical behavior of the $Li[Li_tTi_{1-t}]S_2$ materials

The electrochemical behavior of $Li[Li_tTi_{1-t}]S_2$ materials ($0.17 \leq t \leq 0.33$) presented in Fig. 5 reveals a marked difference between the Li_2TiS_3 end-member and its counterparts with intermediate compositions. Whereas only a small amount of lithium can be removed from Li_2TiS_3 ($t = 0.33$) during the first charge, around 1.1 $Li/Li[Li_tTi_{1-t}]S_2$ are extracted from the other lithium-rich layered sulfides ($t = 0.17, 0.20, 0.25$). This amount is close to the theoretical one $(1 + t)$ $Li/Li[Li_tTi_{1-t}]S_2$ assuming no electronic limitations, and indicates that a significant fraction of Li^+ ions is actually extracted from the $[Li_tTi_{1-t}]S_2$ slabs. An intermediate behavior is observed for the composition $t = 0.29$ for which the capacity at the first cycle is significantly reduced (0.8 Li per formula unit) compared to capacities obtained for lower values of t, while still being significantly higher than what is measured for Li_2TiS_3.

Besides, voltage curves for the first charge exhibit only a single plateau at 2.8 V *vs* Li^+/Li in the case of Li_2TiS_3, whereas two well-defined steps are observed for intermediate compositions ($0.17 \leq t \leq 0.29$), evidenced by a sloping region between 2.3-2.6 V followed by a flat plateau at ~2.8 V which is similar to the one observed for Li_2TiS_3. The number of exchanged electrons (Δx) in the sloping region corresponds to the amount of Ti^{3+} $(1-3t)$ present in the starting materials. These results suggest that the oxidation of initial Ti^{3+} to Ti^{4+} occurs during this first step, followed by the oxidation of S^{2-} anions on the 2.8 V plateau. Note that a very small amount of lithium can be inserted in the pristine materials, indicating the presence of some Li^+ vacant sites and suggesting a spontaneous oxidation of the Ti^{3+} species present at the surface of the material by the electrolyte species, as previously observed for discharged $Li_4Ti_5O_{12}$ electrodes [28,29]. Upon the subsequent discharge, in all cases, lithium is re-intercalated to a composition very close to the initial one, hence with a very low irreversibility. The shape of the discharge curve is significantly different from that of the first charge which is considered as the consequence of an activation phenomenon. Two smooth slopes are observed and are retained over the subsequent charge. Materials recovered after charge and after one cycle were characterized by XRD: in all cases the O3 type structure is maintained. Fig. S2 displays the XRD pattern of the pristine and de-intercalated phase for the $t = 0.25$ material.

As shown in Fig. 6a, first discharge capacities are all about 250 mAh·g^{-1} (corresponding to 585–605 Wh·kg^{-1}) for $t = 0.17, 0.20$ and 0.25 compositions. For t = 0.17, i.e. the sample with the lower amount of 'extra' lithium, the capacity decreases continuously during the cycling from the first cycle. On the contrary, the capacity levels off at a high value for $t = 0.20$ and 0.25 after a small increase is observed during the very first cycles. For higher values of t ($t = 0.29$), the evolution of the capacity is quite different insomuch as the latter increases significantly upon cycling, starting from 150 mAh·g^{-1} at the first cycle up to 265 mAh·g^{-1} by the 50th cycle (Fig. 6a). This behavior illustrates the occurrence of an activation phenomenon which is clearly evidenced in Fig. 7a and Fig. 7b.
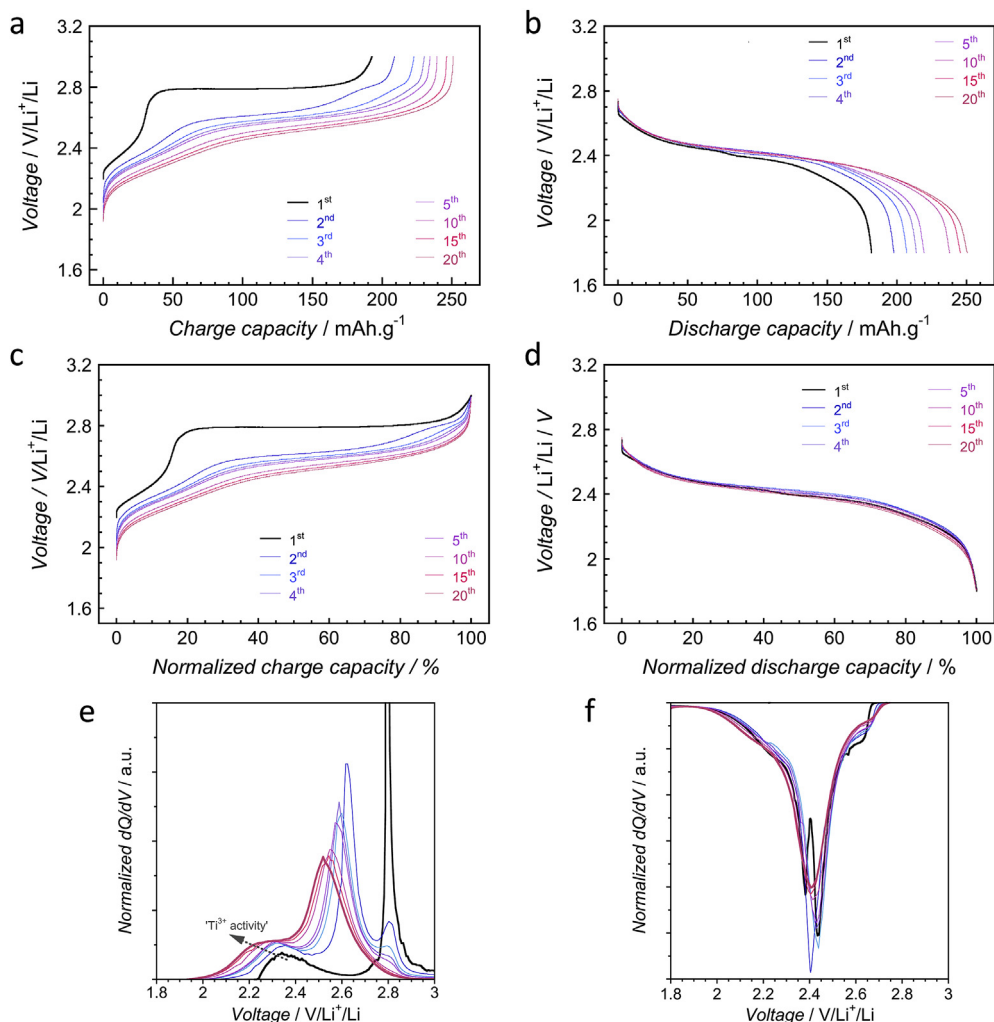
Fig. 7. Electrochemical behavior of $Li[Li_{0.29}Ti_{0.71}]S_2$ cycled at constant current (C/50 rate, 25 °C). (a) Charge (respectively (b) discharge) curves during the first 20 cycles. (c) Corresponding charge ((d) respectively discharge) curves using normalized capacities. (e,f) Corresponding plots of the derivative $\partial(capacity)/\partial(voltage)$.

A similar but slower activation process is also triggered when all Ti ions are originally in the tetravalent state, and thus electrochemically inactive in oxidation, i.e. for Li_2TiS_3 ($Li[Li_{0.33}Ti_{0.67}]S_2$) (Fig. 8). In that case, the first charge curve is exclusively composed of a plateau at 2.8 V, with a corresponding capacity that is limited to 0.15 $Li/Li[Li_{0.33}Ti_{0.67}]S_2$ (35 mAh·g^{-1}), i.e. ~11% of the theoretical one. Then, as shown in Fig. 8a and b, the capacity steadily and slowly increases upon cycling. At the 100th cycle, it reaches 55 and 92 mAh.g^{-1} respectively for C/50 and C/100 current rates (Fig. 6b), showing that this activation process is more dependent on the time and/or the current density than on the cycle number.

Electrochemical measurements performed on $Li[Li_{0.17}Ti_{0.83}]S_2$ illustrate that capacity fade is mainly a consequence of the displacement of the discharge curves towards lower potentials upon cycling (i.e. voltage decay). The evolution of the normalized discharge curves (Fig. 5c,d) of different materials clearly shows that the voltage decay diminishes with the initial increase of Li concentration in the $[Li_tTi_{1-t}]S_2$ slabs ($0.17 < t < 0.25$), before finally leveling off for higher t values ($t = 0.29, 0.33$) (Figs. 7d and 8d).

XPS analyses performed on $Li_{1.25-x}Ti_{0.75}S_2$ de-intercalated materials (Fig. 9a and Table S3a) confirm that the oxidation of S^{2-} and the formation of S_2^{2-} takes place on the 2.8 V plateau. Indeed, S^{2-} species contained in the pristine material remain unchanged in the material charged at 2.6 V, whereas a major amount of $(S_2)^{2-}$ species are present in the material after a charge at 3.0 V. In the case of the Li_2TiS_3 material

charged up to 3 V vs Li^+/Li (first charge (Fig. 9b and Table S3b)), the S2p spectrum is similar to that observed for the almost fully de-intercalated $Li_{1.25-x}Ti_{0.75}S_2$, but with the presence of a slightly higher $(S_2)^{2-}$ content. This similarity, despite the fact that only 0.15 Li per $Li[Li_{0.33}Ti_{0.67}]S_2$ was actually de-intercalated, indicates that near complete delithiation of the $Li[Li_{0.33}Ti_{0.67}]S_2$ material is achieved at the extreme surface of the particles probed by XPS, (approximately 5 nm). To the extent that the activation of the material is proceeding inwards from the surface of the particles, the activation rate of +0.55 mAh.g^{-1}.cycle^{-1} evidenced for the Li_2TiS_3 samples (Fig. 6b), which corresponds to +0.15 vol%.cycle^{-1}, would indicate an average progression of the activation front of few angströms at each cycle for particles of 1–10 μm in diameter. On this assumption, the observed linear evolution of the capacity would be a consequence of the negligible thickness of the newly activated part of the material compared to the radius of the particles, and the change of slope observed after 100–150 cycles could originate from a bimodal particle size distribution (Fig. S3).

A similar surface-confined electronic and/or ionic transport has been evidenced for Li_2MnO_3, which becomes electrochemically active only when in the form of nanoparticles [30]. This behavior suggests a transition in the conductivity of the electrode material upon deintercalation. It is emphasized by the zoom of the charge curves at the beginning of the 2.6 V plateau presented in Fig. S4. This peculiar shape of the voltage curve with a bump is observed for Li_2TiS_3 and $t \geq 0.25$, but is absent for the materials with smaller amounts of lithium in the slabs. Such a shape is
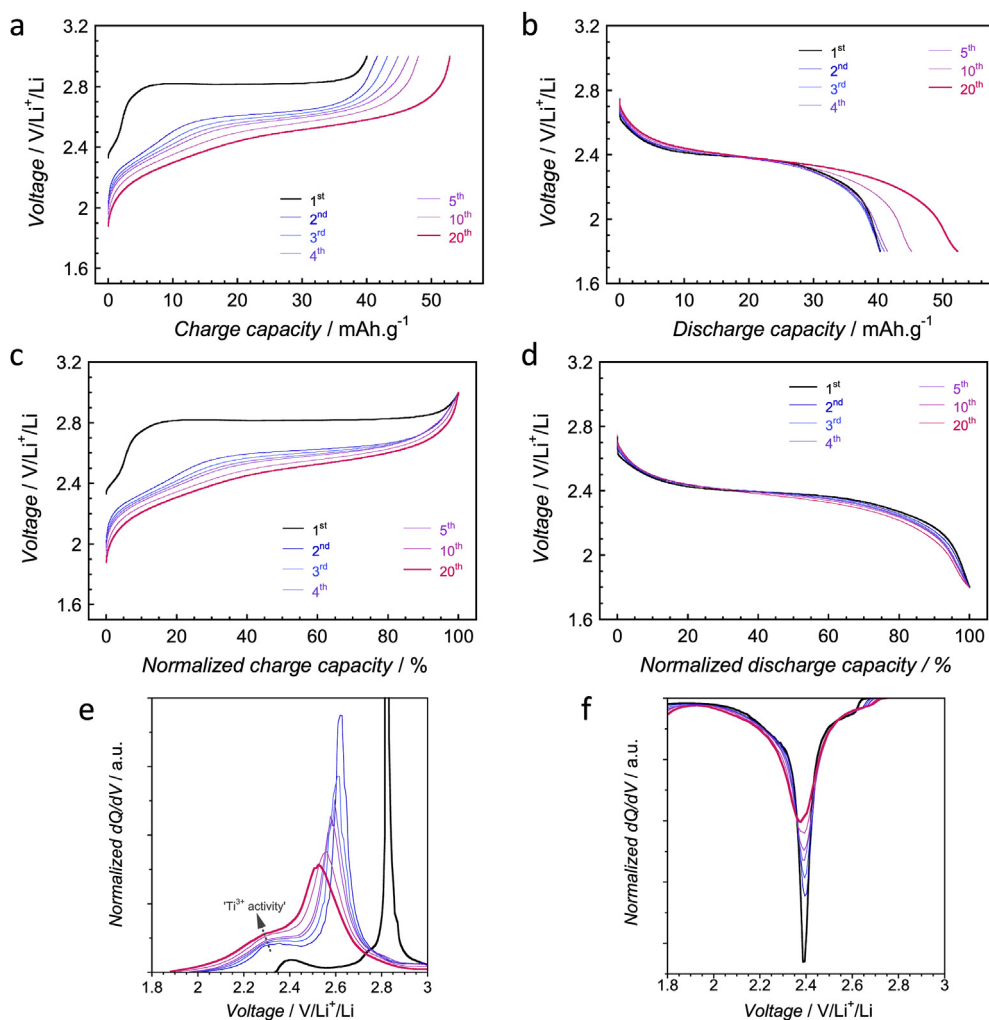
Fig. 8. Electrochemical behavior of Li_2TiS_3 cycled at constant current (C/50 rate, 25 °C). (a) Charge (respectively (b) discharge) curves during the first 20 cycles. (c) Corresponding charge ((d) respectively discharge) curves using normalized capacities. (e, f) Corresponding plots of the derivative ∂(capacity)/∂(voltage).

frequently observed in the Li_xCoO_2 system at the beginning of the first charge [31], as a result of an increase in the electronic conductivity of the material induced by Li^+ deintercalation.

Taken together, the results highlight that the presence of mixed-valence Ti^{3+}/Ti^{4+} species in the pristine layered material facilitates initiation and propagation of the de-intercalation process in the bulk of these lithium-rich layered sulfides. In the case of Li_2TiS_3, Li^+ de-intercalation only leads to the formation of S_2^{2-} species on the surface of the material, which has no direct beneficial effect on the electronic conductivity of the latter.

Finally all the samples $Li[Li_tTi_{1-t}]S_2$ ($t = 0.33$, 0.29, 0.25, 0.20 and 0.17) display very low irreversible capacity after the first cycle. This appears as a marked difference when compared to conventional Li-rich oxides, where oxygen oxidation occurs simultaneously both in the bulk and on particle surfaces leading to oxygen evolution from the surface and concomitantly to a partial reaction with the liquid electrolyte to form CO_2 [32,33]. It is noted that the irreversible capacity in oxides can be reduced either by the presence of Li vacancies in the pristine material obtained via an optimized synthesis [34,35], or with the chemical pre-activation of the material by hydrazine treatment [36]. In the case of sulfides, the oxidation of S^{2-}, which occurs at 2.8 V vs Li^+/Li, is much easier; hence, there is no tendency to form S^0 at the surface of the particles. Besides, contrary to oxides, the oxidation of sulfide anions occurs in the electrochemical stability window of the electrolyte and even if the formation and dissolution of poly-sulfides cannot be excluded, the latter has little influence since the capacity is very stable upon cycling.

A specific experiment was carried out with $Li[Li_{0.20}Ti_{0.80}]S_2$ to observe the impact of the activation on the two supposedly separated Ti^{3+}/Ti^{4+} and S^{2-}/S_2^{2-} redox processes. The material was discharged at first to 1.6 V vs Li^+/Li, then cycled four times in the 1.6–2.6 V vs Li^+/Li voltage range corresponding to the redox activity of the sole Ti species, and finally cycled in the full 1.6–3.0 V vs Li^+/Li range (Fig. 10). The 4 cycles performed in the 1.6–2.6 V vs Li^+/Li range highlights the perfect reversibility of the redox process in which the Ti^{3+}/Ti^{4+} couple is involved. Once the material is charged to 3 V vs Li^+/Li, the next discharge
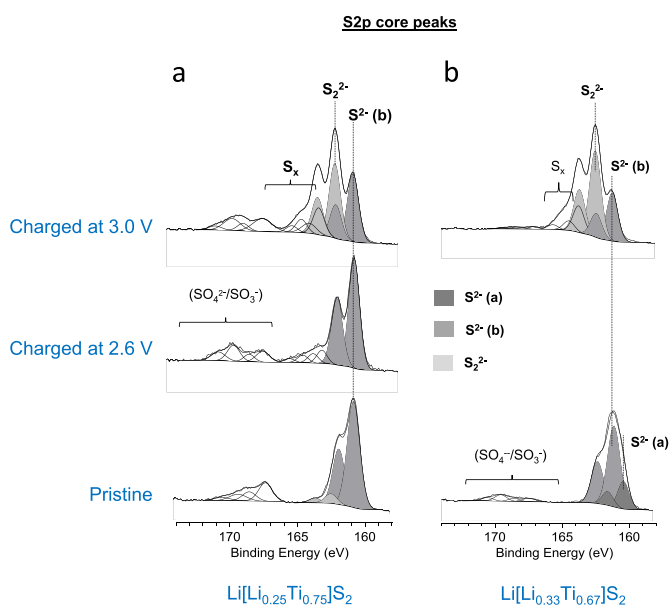
presents a classical S shape and an overlap between several phenomena which is evidenced in the plot of $\partial Q/\partial V$ vs V (Fig. 10b). This experiment shows that during the first charge the titanium oxidation and the activation phenomenon associated with the sulfur oxidation are well separated. During the second charge, there is a strong decrease of the polarization and an overlap between different phenomena: the classical Ti^{3+}/Ti^{4+} oxidation remains, but another process appears at a slightly higher voltage.

3.3. General discussion

Based on electrochemical measurements and XPS analyses, a general scheme of the various involved phenomena can be proposed. When cycling is confined in the 1.8–2.6 V range, only the classical redox process involving the $Ti^{3+/4+}$ couple occurs. This reaction is fully reversible as shown by the red curve of Fig. 10a, and the composition of $Li_{4t}Ti_{1-t}S_2$ for which all titanium ions are in the tetravalent state is thus the limit of this reversible range. When de-intercalation is continued at higher voltages, then oxidation of S^{2-} ions takes place along the 2.8 V plateau. S^- ions are then formed by similarity with the overlithiated layered oxides. As shown by Ceder et al., the presence of Li^+ ions in the transition metal slabs that do not share orbitals with oxygen atoms leads to the formation of an unhybridized state overlapping the cationic bands [37]. For oxides with 3d elements only O^- ions are formed, while in the case of 4d elements there is formation of $(O=O)^{2-}$ pairs [38–40] thanks to the covalence increase which allows for reductive coupling to occur, as it has been proposed by Doublet et al. [41,42]. An O^- and an O^{2-} belonging to an MO_6 octahedron make a bond to form an $(O_2)^{2-}$ ion while an electron is sent back to the M cation which is then reduced.

In the case of sulfides, the tendency to form S_2^{2-} persulfide ions via the reductive coupling reaction, even for 3d transition metal, is enhanced by the covalent character of the bonds. The effect of the covalency on the formation of S_2^{2-} pairs was discussed by Rouxel in the case of the 3d MS_2 materials [43,44]. On the left of the periodic classification the MS_2 phases are built up M^{4+} and S^{2-} ions, while on the right, thanks to the increase of covalency, they are built up of M^{2+} and S_2^{2-}.

In the particular case of the overlithiated lithium layered sulfides, the presence of lithium in the slab increases the covalency of the antagonist Ti–S bonds. Therefore, both the presence of non-bonded 3p sulfur orbitals and the increase in Ti–S bond covalency facilites the S^{2-} oxidation and the reductive coupling phenomenon. The reaction can be summarized in the following way: $Ti^{4+}(S^{2-})_6$ is oxidized to $Ti^{4+}(S^{2-})_5S^-$ in a first step when a Li^+ ion is deintercalated; then the reductive coupling occurs leading to $Ti^{3+}(S^{2-})_4(S_2^{2-})$. This reaction occurs in priority on the S^{2-} surrounding a Li^+ ion or a vacancy in the $[Ti,Li,\square]S_2$ slabs. In Li_2TiS_3, the $Li_{1/3}Ti_{2/3}S_2$ slab is formed of edge-sharing $Ti^{4+}(S^{2-})_6$ and $Li^+(S^{2-})_6$ octahedra with a honeycomb ordering (Fig. S5a). Upon Li de-intercalation (Fig. S5b), S^{2-} ions are oxidized as described above with formation in a first step of $Ti^{3+}(S^{2-})_4(S_2^{2-})$ entities which are further oxidized to $Ti^{3+}(S_2^{2-})_3$ at the end of the de-intercalation (Fig. S5c). For intermediate compositions ($Li[Li_tTi_{1-t}]S_2$ ($0.10 < t < 0.33$), the mechanism is more complex given the variety of pristine environments for Li^+ and $Ti^{3+/4+}$ ions, as illustrated in Fig. S5d by their schematic distribution for the case of a $[Li_{0.20}Ti_{0.80}]S_2$ slab (t = 0.2). In the related fully delithiated slab ($Ti_{0.8}\square_{0.2}S_2$), there are several surroundings for Ti ions, represented by several colors in Figs. S5e and f, depending on the adjoining Li^+ ions (or the vacancies). In this scheme, the S_2^{2-} species are localized around the titanium surrounded by 3, 2 or 1 vacancies. One can assume that in the domains which exhibit a Ti_2S_3 type surrounding, the S^{2-} oxidation is easier because all sulfide ions tend to be oxidized ($Ti^{3+}(S^{2-})_4(S_2^{2-})$ pink octahedra). In some other parts of the lattice, where vacancies are absent or sufficiently distant, titanium ions will be surrounded by sulfide ions that are not involved in persulfide entities, like in TiS_2. As a consequence, the latter will remain in the tetravalent state: ($Ti^{4+}(S^{2-})_6$ yellow octahedra). The other titanium ions (3 + or 4+) are surrounded by S^{2-}, S_2^{2-} and S^- belonging to S_2^{2-}. In discharge, both

S2p core peaks

Charged at 3.0 V

Charged at 2.6 V

Pristine

$Li[Li_{0.25}Ti_{0.75}]S_2$

$Li[Li_{0.33}Ti_{0.67}]S_2$

Fig. 9. Oxidation of the anion during the charge. (a) XPS S2p core spectra of the pristine $Li[Li_{0.25}Ti_{0.75}]S_2$ sample and of similar electrodes independently charged at 2.6 and 3 V. The S2p core spectrum mainly consists of a doublet corresponding to S^{2-} (161.0–162.2 eV). The new doublet appearing at higher binding energy for the sample charged at 3 V is due to S_2^{2-} disulfide species associated with anion contribution to the redox process. (b) XPS S2p core spectra of the pristine $Li[Li_{0.33}Ti_{0.67}]S_2$ sample and of the corresponding electrode charged at 3 V.
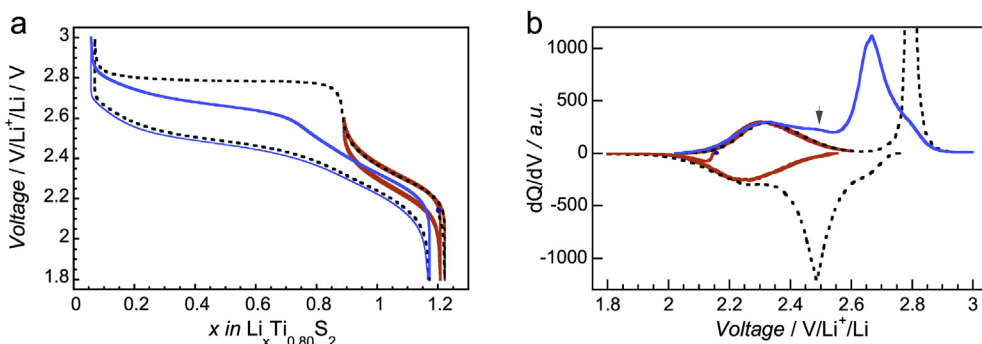
Fig. 10. Electrochemical behavior of Li [Li$_{0.20}$Ti$_{0.80}$]S$_2$. (a) Voltage profiles for the Li [Li$_{1+t}$Ti$_{1-t}$]S$_2$ (t = 0.20) material in a lithium metal cell. The first four cycles performed in the voltage range [1.8–2.6] V *vs* Li$^+$/Li are represented in red. The subsequent first full cycle is represented in black dotted line and the next one in blue. (b) Corresponding plot of the derivative ∂(capacity)/∂V. Arrow indicates the presence of a new oxidation step at ~2.5 V assigned to the presence of extra Ti^{3+} in the discharged 'activated' material. (For interpretation of the references to color in this figure legend, the reader is referred to the Web version of this article.)

Ti^{4+} and S$_2^{2-}$ species are reduced to reach an overall composition close to the initial one. Nevertheless, after the first charge activation, the shape of the curves is very similar in charge and in discharge. This shows that after the first discharge the electron distribution has changed compared to the one present in the pristine material. One can make the hypothesis of remaining stable S$_2^{2-}$ bound to Ti^{3+} ions leading to a general formula Li$_{1+y}$[Ti^{3+}, Ti^{4+}, S^{2-}, S$_2^{2-}$]. The presence of S$_2^{2-}$ species in the reintercalated material leads to an increase of the amount of Ti^{3+} compared to the pristine material. Their oxidation leads to the bump at 2.5 V during the subsequent charge in addition to the 2.3 V peak on the ∂Q/∂V curve of Fig. 10b. During the subsequent discharge (and in the following cycles), overlap between the Ti^{3+}/Ti^{4+} and the S^{2-}/(S$_2$)$^{2-}$ redox couples suppresses this polarization.

4. Conclusion

In summary, a series of lithium-rich layered phases belonging to the LiTiS$_2$ - Li$_2$TiS$_3$ system has been synthesized. These Co- and Ni-free materials exhibit an electrochemical behavior analogous to the Li-rich (Co,Ni, Mn) layered oxide systems: (i) activation process during the first charge, (ii) participation of anions to the redox processes, and (iii) very large reversible capacity. Energy densities higher than 600 Wh.kg^{-1} are reached, despite a lower cell voltage compared to oxides that originates from the strong covalent character of the bonds. In these Li-rich sulfides, easy oxidation of S^{2-} ions to (S$_2$)$^{2-}$ prevents sulfur extraction (in contrast with oxygen evolution for oxides). As a result, the irreversible capacity is negligible and there is almost no material densification on the particle surface. Moreover, the covalent character of the bonds inhibits material destabilization in the fully de-intercalated state, which limits the capacity loss and the voltage decay. Finally, the combination of a high energy density, an operating voltage compatible with the electrochemical stability window of sulfur based solid electrolytes and the absence of critical elements in their compositions, makes some of these new phases interesting candidates for positive electrode material in high energy solid state batteries.

Author contributions section

Florian Flamary: Investigation, Vizualisation, Writing original draft. **Adrien Boulineau**: Investigation, Vizualisation. **Hervé Martinez**: Investigation, Vizualisation, Writing original draft. **Matthew Suchomel**: Investigation, Vizualisation, Writing original draft. **Claude Delmas**: Conceptualization, Vizualisation, Writing original draft, Writing – Review & Editing. **Brigitte Pecquenard**: Supervision, Conceptualization, Writing original draft, Writing – Review & Editing. **Frédéric Le Cras**: Supervision, Funding acquisition, Conceptualization, Vizualisation, Writing – original draft, Writing – Review & Editing.

Declaration of competing interest

The authors declare no conflict of interest.

Appendix A. Supplementary data

Supplementary data to this article can be found online at https://doi.org/10.1016/j.ensm.2019.12.033.

References

[1] E.A. Olivetti, G. Ceder, G.G. Gaustad, X. Fu, Lithium-ion battery supply chain considerations: analysis of potential bottlenecks in critical metals, Joule 1 (2017) 229–243, https://doi.org/10.1016/j.joule.2017.08.019.

[2] D. Andre, S.-J. Kim, P. Lamp, S.F. Lux, F. Maglia, O. Paschos, B. Stiaszny, Future generations of cathode materials: an automotive industry perspective, J. Mater. Chem. A 3 (2015) 6709–6732, https://doi.org/10.1039/C5TA00361J.

[3] N. Kamaya, K. Homma, Y. Yamakawa, M. Hirayama, R. Kanno, M. Yonemura, T. Kamiyama, Y. Kato, S. Hama, K. Kawamoto, A. Mitsui, A lithium superionic conductor, Nat. Mater. 10 (2011) 682–686, https://doi.org/10.1038/nmat3066.

[4] Y. Kato, S. Hori, T. Saito, K. Suzuki, M. Hirayama, A. Mitsui, M. Yonemura, H. Iba, R. Kanno, High-power all-solid-state batteries using sulfide superionic conductors, Nat. Energy 1 (2016) 16030, https://doi.org/10.1038/nenergy.2016.30.

[5] K.H. Park, Q. Bai, D.H. Kim, D.Y. Oh, Y. Zhu, Y. Mo, Y.S. Jung, Design strategies, practical considerations, and new solution processes of sulfide solid electrolytes for all-solid-state batteries, Adv. Energy Mater. 8 (2018), https://doi.org/10.1002/aenm.201800035, 1800035.

[6] W.D. Richards, L.J. Miara, Y. Wang, J.C. Kim, G. Ceder, Interface stability in solid-state batteries, Chem. Mater. 28 (2016) 266–273, https://doi.org/10.1021/acs.chemmater.5b04082.

[7] G.F. Dewald, S. Ohno, M.A. Kraft, R. Koerver, P. Till, N.M. Vargas-Barbosa, J. Janek, W.G. Zeier, Experimental assessment of the practical oxidative stability of lithium thiophosphate solid electrolytes, Chem. Mater. 31 (2019) 8328–8337, https://doi.org/10.1021/acs.chemmater.9b01550.

[8] W.J. Li, M. Hirayama, K. Suzuki, R. Kanno, Fabrication and electrochemical properties of a LiCoO$_2$ and Li$_{10}$GeP$_2$S$_{12}$ composite electrode for use in all-solid-state batteries, Solid State Ion. 285 (2016) 136–142, https://doi.org/10.1016/j.ssi.2015.05.007.

[9] F. Flamary-Mespoulie, Synthèse et caractérisation de sulfures de métaux de transition comme matériaux d'électrode positive à forte capacité pour microbatteries au lithium, PhD Thesis, University of Bordeaux, 2016, https://tel.archives-ouvertes.fr/tel-01673794/document.

[10] D.W. Murphy, F.J. Di Salvo, G.W. Hull, J.V. Waszczak, Convenient preparation and physical properties of lithium intercalation compounds of Group 4B and 5B layered transition metal dichalcogenides, Inorg. Chem. 15 (1976) 17–21, https://doi.org/10.1021/ic50155a005.

[11] M.S. Whittingham, The role of ternary phases in cathode reactions, J. Electrochem. Soc. 123 (1976) 315–320, https://doi.org/10.1149/1.2132817.

[12] M.S. Whittingham, F.R. Gamble, The lithium intercalates of the transition metal dichalcogenides, Mater. Res. Bull. 10 (1975) 363–372, https://doi.org/10.1016/0025-5408(75)90006-9.

[13] K. Selte, E. Bjerkelund, A.J. Kjekshus, Intermediate phases in the systems niobium-selenium, niobium-tellurium, tantalum-selenium, and tantalum-tellurium, Less-Common Metals 11 (1966) 14–30, https://doi.org/10.1016/0022-5088(66)90053-1.

[14] C. Delmas, C. Fouassier, P. Hagenmuller, Structural classification and properties of the layered oxides, Physica 99B (1980) 81, https://doi.org/10.1016/0378-4363(80)90214-4.

[15] K.M. Colbow, J.R. Dahn, R.R. Haering, The 3R phase of Li_xTiS_2, J. Power Sources 26 (1989) 301–307, https://doi.org/10.1016/0378-7753(89)80138-7.

[16] D. Wiedemann, S. Nakhal, A. Senyshyn, T. Bredow, The high-temperature transformation from 1T- to 3R-Li_xTiS_2 (x = 0.7, 0.9) as observed in situ with neutron powder diffraction, M. Z. Lerch, Phys. Chem. 229 (2015) 1275–1288, https://doi.org/10.1515/zpch-2014-0659.

[17] J.A. Brant, D.M. Massi, N.A.W. Holzwarth, J.H. Macneil, A.P. Douvalis, T. Bakas, S.W. Martin, M.D. Gross, J.A. Aitken, Fast lithium ion conduction in Li_2SnS_3: synthesis, physicochemical characterization, and electronic structure, Chem. Mater. 27 (2015) 189–196, https://doi.org/10.1021/cm503752.

[18] F. Lissner, T.Z. Schleid, Na_2ZrS_3: Ein ternäres sulfid des zirconiums mit aufgefüllter $AlCl_3$-struktur, Anorg. Allg 625 (1999) 195–196, https://doi.org/10.1002/(SICI)1521-3749(199902)625, 2%3C195::AID-ZAAC195%3E3.0.CO;2-V.

[19] H. Masuda, T. Fujino, N. Sato, K. Yamada, M. Wakeshima, Synthesis and crystal structure of alkali metal uranium sulfides, Li_2US_3 and Na_2US_3, J. Alloy. Comp. 284 (1999) 117–123, https://doi.org/10.1016/S0925-8388(98)00920-7.

[20] A. Sakuda, T. Takeuchi, K. Okamura, H. Kobayashi, H. Sakaebe, K. Tatsumi, Z. Ogumi, Rock-salt-type lithium metal sulfides as novel positive-electrode materials, Sci. Rep. 4 (2014) 4883, https://doi.org/10.1038/srep04883.

[21] F. Le Cras, B. Pecquenard, V. Dubois, V.P. Phan, D. Guy-Bouyssou, All-solid-state lithium-ion microbatteries using silicon nanofilm anodes: high performance and memory effect, Adv. Energy Mater. 5 (2015) 1501061, https://doi.org/10.1002/aenm.201501061.

[22] V. Dubois, B. Pecquenard, S. Soulé, H. Martinez, F. Le Cras, Dual cation- and anion-based redox process in lithium titanium sulphide thin film cathodes for all-solid-state lithium-ion batteries, ACS Appl. Mater. Interfaces 9 (2017) 2275–2284, https://doi.org/10.1021/acsami.6b11987.

[23] J. Rodriguez-Carvajal, Physica B 192 (1993) 55–69, https://doi.org/10.1016/0921-4526(93)90108-I.

[24] A. Boulineau, L. Croguennec, C. Delmas, F. Weill, Reinvestigation of Li_2MnO_3 structure: electron diffraction and high resolution TEM, Chem. Mater. 21 (2009) 4216–4222, https://doi.org/10.1021/cm900998n.

[25] M.H. Lindic, H. Martinez, A. Benayad, B. Pecquenard, P. Vinatier, A. Levasseur, D. Gonbeau, XPS investigations of TiO_yS_z amorphous thin films used as positive electrode in lithium microbatteries, Solid State Ion. 176 (2005) 1529–1537, https://doi.org/10.1016/j.ssi.2005.04.007.

[26] C. Didier, M. Guignard, C. Denage, O. Szajwaj, S. Ito, I. Saadoune, J. Darriet, C. Delmas, Electrochemical Na-deintercalation from $NaVO_2$, Electrochem. Solid State Lett. 14 (2011) A75–A78, https://doi.org/10.1149/1.3555102.

[27] C. Didier, M. Guignard, J. Darriet, C. Delmas, O'3-Na_xVO_2 system: a superstructure for $Na_{1/2}VO_2$, Inorg. Chem. 51 (2012) 11007–11016, https://doi.org/10.1021/ic301505e.

[28] X. Lu, L. Gu, Y.S. Hu, H.C. Chiu, H. Li, G.P. Demopoulos, L. Chen, New insight into the atomic-scale bulk and surface structure evolution of $Li_4Ti_5O_{12}$ anode, J. Am. Chem. Soc. 137 (2015) 1581–1587, https://doi.org/10.1021/ja5115562.

[29] J.B. Gieu, C. Courrèges, L. El Ouatani, C. Tessier, H. Martinez, Temperature effects on $Li_4Ti_5O_{12}$ electrode/electrolyte interfaces at the first cycle: a X-ray photoelectron spectroscopy and scanning Auger microscopy study, J. Power Sources 318 (2016) 291–301, https://doi.org/10.1016/j.jpowsour.2016.04.007.

[30] S.F. Amalraj, D. Sharon, M. Talianker, C.M. Julien, L. Burlaka, R. Lavi, E. Zhecheva, B. Markovsky, E. Zinigrad, D. Kovacheva, R. Stoyanova, D. Aurbach, Study of the nanosized Li_2MnO_3: electrochemical behavior, structure, magnetic properties, and vibrational modes, Electrochim. Acta 97 (2013) 259–270, https://doi.org/10.1016/j.electacta.2013.03.029.

[31] M. Ménétrier, D. Carlier, M. Blangero, C. Delmas, On 'really' stoichiometric $LiCoO_2$, Electrochem. Solid State Lett. 11 (2008) A179–A182, https://doi.org/10.1149/1.2968953.

[32] A.R. Armstrong, M. Holzapfel, P. Novák, C.S. Johnson, S.-H. Kang, M.M. Thackeray, P.G. Bruce, Demonstrating oxygen loss and associated structural reorganization in the lithium battery cathode $Li[Ni_{0.2}Li_{0.2}Mn_{0.6}]O_2$, J. Am. Chem. Soc. 128 (2006) 8694–8698, https://doi.org/10.1021/ja062027+.

[33] F. La Mantia, F. Rosciano, N. Tran, P. Novák, Quantification of oxygen loss from $Li_{1+x}(Ni_{1/3} Mn_{1/3} Co_{1/3})_{1-x}O_2$ at high potentials by differential electrochemical mass spectrometry, J. Electrochem. Soc. 156 (2009) A823–A827, https://doi.org/10.1149/1.3205495.

[34] R. Shunmugasundaram, R. Senthil Arumugam, J.R. Dahn, High capacity Li-rich positive electrode materials with reduced first-cycle irreversible capacity loss, Chem. Mater. 27 (2015) 757–767, https://doi.org/10.1021/cm504583y.

[35] R. Shunmugasundaram, R. Senthil Arumugam, K.J. Harris, G.R. Goward, J.R. Dahn, A search for low-irreversible capacity and high-reversible capacity positive electrode materials in the Li-Ni-Mn-Co pseudoquaternary system, Chem. Mater. 28 (2016) 55–66, https://doi.org/10.1021/acs.chemmater.5b02104.

[36] P. Oh, M. Ko, S. Myeong, Y. Kim, J. Cho, A novel surface treatment method and new insight into discharge voltage deterioration for high-performance $0.4Li_2MnO_3$-$0.6LiNi_{1/3}Co_{1/3}Mn_{1/3}O_2$ cathode materials, Adv. Energy Mater. 4 (2014), https://doi.org/10.1002/aenm.201400631, 1400631.

[37] D.-H. Seo, J. Lee, A. Urban, R. Malik, S. Kang, G. Ceder, The structural and chemical origin of the oxygen redox activity in layered and cation disordered Li excess cathode materials, Nat. Chem. 8 (2016) 692–697, https://doi.org/10.1038/nchem.2524.

[38] M. Sathiya, G. Rousse, K. Ramesha, C.P. Laisa, H. Vezin, M.T. Sougrati, M.-L. Doublet, D. Foix, D. Gonbeau, W. Walker, A.S. Prakash, M. Ben Hassine, L. Dupont, J.-M. Tarascon, Reversible anionic redox chemistry in high-capacity layered-oxide electrodes, Nat. Mater. 12 (2013) 827–835, https://doi.org/10.1038/nmat3699.

[39] M. Sathiya, A.M. Abakumov, D. Foix, G. Rousse, K. Ramesha, M. Saubanère, M.-L. Doublet, H. Vezin, C.P. Laisa, A.S. Prakash, D. Gonbeau, G. VanTendeloo, J.-M. Tarascon, Origin of voltage decay in high-capacity layered oxide electrodes, Nat. Mater. 14 (2015) 230–238, https://doi.org/10.1038/nmat4137.

[40] C. Delmas, Operating through oxygen, Nat. Chem. 8 (2016) 641–643, https://doi.org/10.1038/nchem.2558.

[41] M. Saubanère, E. McCalla, J.-M. Tarascon, M.-L. Doublet, The intriguing question of anionic redox in high-energy density cathodes for Li-ion batteries, Energy Environ. Sci. 9 (2016) 984–991, https://doi.org/10.1039/C5EE03048J.

[42] Y. Xie, M. Saubanère, M.-L. Doublet, Requirements for reversible extra-capacity in Li-rich layered oxides for Li-ion batteries, Energy Environ. Sci. 10 (2017) 266–274, https://doi.org/10.1039/C6EE02328B.

[43] J. Rouxel, Anion-cation redox competition and the formation of new compounds in highly covalent systems, Chem. Eur J. 2 (1996) 1053–1059, https://doi.org/10.1002/chem.19960020904.

[44] S. Jobic, R. Brec, J. Rouxel, Occurrence and characterization of anionic bondings in transition metal chalcogenides, J. Alloy. Comp. 178 (1992) 253–283, https://doi.org/10.1016/0925-8388(92)90269-F.